

# Derivation of attenuation map for attenuation correction of PET data in the presence of nanoparticulate contrast agents using spectral CT imaging

Hossein Ghadiri · Mohammad Bagher Shiran ·  
Hamid Soltanian-Zadeh · Arman Rahmim ·  
Habib Zaidi · Mohammad Reza Ay

Received: 2 December 2013 / Accepted: 20 March 2014 / Published online: 9 April 2014  
© The Japanese Society of Nuclear Medicine 2014

## Abstract

**Objective** Uptake value in quantitative PET imaging is biased due to the presence of CT contrast agents when using CT-based attenuation correction. Our aim was to examine spectral CT imaging to suppress inaccuracy of 511 keV attenuation map in the presence of multiple nanoparticulate contrast agents.

**Methods** Using a simulation study we examined an image-based K-edge ratio method, in which two images acquired from energy windows located above and below the K-edge energy are divided by one another, to identify the exact location of all contrast agents. Multiple computerized phantom studies were conducted using a variety of NP contrast agents with different concentrations. The performance of the proposed methodology was compared to conventional single-kVp and dual-kVp methods using wide range of contrast agents with varying concentrations.

**Results** The results demonstrate that both single-kVp and dual-kVp energy mapping approaches produce inaccurate attenuation maps at 511 keV in the presence of multiple simultaneous contrast agents. In contrast, the proposed method is capable of handling multiple simultaneous contrast agents, thus allowing suppression of 511 keV attenuation map inaccuracy.

**Conclusion** Attenuation map produced by spectral CT clearly outperforms conventional single-kVp and dual-kVp approaches in the generation of accurate attenuation maps in the presence of multiple contrast agents.

**Keywords** PET/CT · Nanoparticulate contrast agents · K-edge imaging · Multi-energy spectral CT

---

H. Ghadiri · M. R. Ay (✉)  
Department of Medical Physics and Biomedical Engineering,  
Tehran University of Medical Sciences, Tehran, Iran  
e-mail: mohammadreza\_ay@tums.ac.ir;  
mohammadreza\_ay@sina.tums.ac.ir

H. Ghadiri · M. R. Ay  
Research Center for Molecular and Cellular Imaging,  
Tehran University of Medical Sciences, Tehran, Iran

M. B. Shiran  
Department of Medical Physics, Iran University of Medical  
Sciences, Tehran, Iran

H. Soltanian-Zadeh  
CIPCE, Department of Electrical and Computer Engineering,  
University of Tehran, Tehran, Iran

H. Soltanian-Zadeh  
Department of Radiology, Henry Ford Health System,  
Detroit, MI, USA

A. Rahmim  
Department of Radiology, Johns Hopkins University,  
Baltimore, MD, USA

H. Zaidi  
Division of Nuclear Medicine, Geneva University Hospital,  
Geneva, Switzerland

H. Zaidi  
Geneva Neuroscience Center, Geneva University,  
Geneva, Switzerland

H. Zaidi  
Department of Nuclear Medicine and Molecular Imaging,  
University of Groningen, University Medical Center Groningen,  
Groningen, The Netherlands

## Introduction

The quantitative accuracy of PET images when using CT-based attenuation correction (CTAC) might be compromised in some cases. For instance, CT contrast agents with high atomic numbers, used for enhancing CT images, pose noticeable challenges in the context of CTAC, usually leading to visible artifacts and overestimated PET tracer uptake and inaccurate quantitative PET images [1, 2]. Meanwhile, nanoparticulate (NP) CT contrast agents with high atomic numbers, such as bismuth [3, 4], gold [5–7], platinum [8], tungsten [9], tantalum [10], hafnium [11, 12], lutetium [13], ytterbium [14], erbium [15], and gadolinium [16], have received considerable attention in recent years owing to their higher diagnostic efficacy compared to current contrast agents [17]. The availability of such NP contrast agents opens up unique opportunities for molecular CT imaging, and furthermore, offers the possibility to explore the use of several contrast agents simultaneously to increase the efficiency of diagnostic procedures in a single scan [6, 7, 17, 18]. However, the lack of proper discrimination of contrast agents from bone tissue can lead to noticeable artifacts, [19–22] and upward bias [1] in SUV values via the CTAC procedure. This occurs because contrast agent regions are mistakenly segmented as bone and then mapped accordingly from the CT energy to PET energy [23]. Consequently, to obtain accurate quantitative PET images, resolving the problem of correct differentiation of contrast agent before the energy mapping procedure is of very high importance [24]. However, most energy mapping algorithms based on single-energy(single-kVp) CT exhibit some level of uncertainty in mapping of contrast agent regions [25, 26].

To improve the capability of material differentiation, Spectral CT was introduced: the preliminary concept, in which the X-ray spectrum was subdivided into two energy bins, was proposed by Alvarez and Macovski [27], and subsequently dual-kVp CT based on scanning at two different X-ray spectra was proposed by Lehmann et al. [28]. The latter concept has been improved upon in recent years as dual-source [29], fast kVp switching [30], and dual-layer detector [31] CT systems. Multi-energy CT with energy-sensitive detection systems has been under active investigation in recent years [32–42]. Unlike current clinical CT detectors (single-kVp or dual-kVp), which normally operate in the integral mode, multi-energy CT utilizes energy-sensitive detectors. In multi-energy CT the acquired data are sorted into energy bins according to the energy of each incoming photon. Data gathered in each bin can be separately used for image reconstruction. Due to recent technological improvements in detector design, in terms of energy resolution and speed, it is expected that multi-energy computed tomography can be realized in the clinic [33, 43, 44].

The idea of contrast agent differentiation by use of the K-edge was first introduced by Riederer and Mistretta [45] and further investigated recently by others [32, 36–38, 40]. All these works were performed in projection (sinogram) space and are based on solving systems of simultaneous equations as formed by using multi-energy measurements. A similar concept was investigated by Le and Molloy [34] in the image space. However, designing an appropriate system of simultaneous equations to avoid ill-conditioning, iterative divergence, and using fast and robust methods to solve such systems appears challenging and is still an active research area [35].

In this study, we used a previously proposed image-based K-edge imaging algorithm with the abilities to identify and discriminate multiple contrast agents [46] to minimize contrast-related artifact in hybrid imaging such as PET/CT or SPECT/CT. We aim to address the challenge of using CT images for attenuation correction of nuclear medicine (PET or SPECT) data in the presence of multiple high atomic number CT contrast agents, while providing a straightforward and practical energy mapping algorithm by using analytic simulation.

## Materials and methods

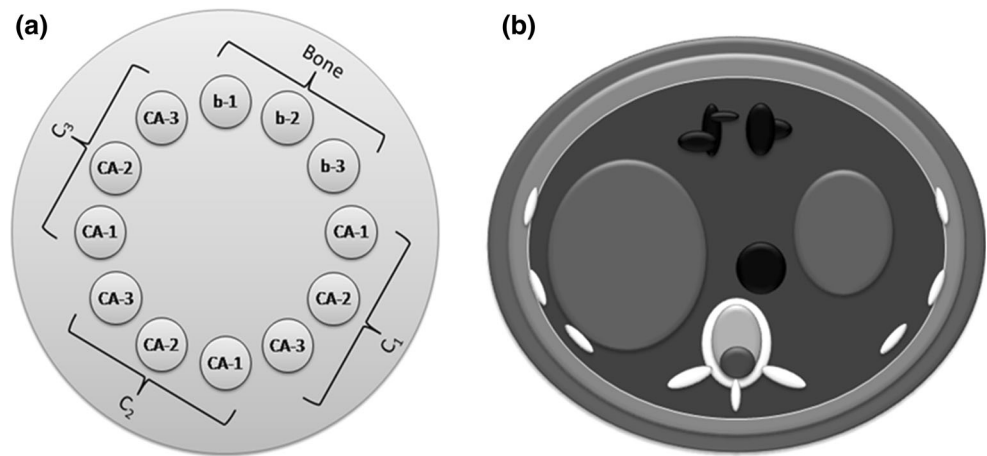
### Analytic CT simulator

We used a sinogram-based analytical model implemented in our center to simulate the complete chain of CT data acquisition. Our model includes the capability of X-ray spectrum generation according to the values of kVp, mAs, inherent and added filter, and slice thickness. The detection system is able to work in either integral (current) or spectral (pulse) modes.

In our model the initial X-ray spectrum was calculated using aluminum equivalent X-ray tube filtration, collimator opening  $A$  ( $\text{mm}^2$ ) (which varies with slice thickness), X-ray tube current–time mAs, and potential kVp based on data obtained from IPEM report 78 [47]. A detector arc consisting of 725 elements (consistent with a  $512 \times 512$  image matrix with 1 mm pixel size) was used and the projections were generated in  $0.4^\circ$  increments along full rotation. Thus, in our model the generated projection matrix of analytically designed computerized phantoms (presented in the next section) consists of  $725 \times 900$  pixels.

The geometrical parameters have been set to be very similar to the clinical CT systems. The X-ray tube focal spot to iso-center and to detector distances have been set to 540 and 950 mm, respectively. The fan angle has been set to  $56^\circ$  which is consistent with 1.02 mm width for each element of the 1D array detector arc. No collimator has

**Fig. 1 a** A scheme of computerized multi-contrast phantom containing three concentrations (*C1*, *C2*, *C3*) of three different contrast agents (*CA-1*, *CA-2*, and *CA-3*), coupled with three concentrations of  $K_2HPO_4$  (*b-1*, *b-2*, and *b-3*). **b** Anthropomorphic phantom, consisting of fat, muscle, liver, stomach, intestine, bone (cortical and trabecular), and aorta



been used in front of the detector, which means that our model has not considered the Compton scattered photons that originated from other ray paths.

To acquire the matrix of detected photon intensities, we used general attenuation function when the calculated initial X-ray spectrum, obtained projection matrix of computerized phantoms, and response function of the detector were used in the calculation. Quantum noise fluctuation of detected signals was simulated by invoking Poisson distribution with a mean of detected photon intensities.

A software procedure of water calibration was designed in the simulation program to measure the extent of beam hardening along the projections. To this end, we designed a computerized 250 mm diameter cylindrical water phantom to obtain beam-hardening correction factors. In the smoothed reconstructed image of the water phantom, the rate of decrease in the pixel values moving from the edge to the center of water phantom was extracted. A first-order linear least square fitting was used to generate a function which represents the profile intensity variation versus phantom depth. The slope and intercept of the obtained linear function was recorded in the calibration file. In the imaging procedure of the simulation program, these parameters are used to correct beam-hardening effects in the projection domain. For each CT parameter that may have different X-ray characteristics, such as filter and kVp value, an individual calibration file was considered.

For image reconstruction, we simply used MATLAB (MathWorks, Inc., Natick, MA) functions of fan beam filtered-back-projection to reconstruct the calculated line integrals as a  $512 \times 512$  image size.

In the integral detection mode, photon energies ranging from 1 keV to maximum value, which normally equals to the kVp values, were taken into account. In the spectral (multi-energy) detection mode, the photons of each energy bin were separately used for image reconstruction.

We validated our code by comparing with experimental data. More details regarding our analytic CT simulator and experimental validation have been reported previously [46, 48].

#### Phantoms and materials

Two shape-based computerized phantoms were designed in the simulation code: first, a water-filled multi-contrast phantom with 12 cavities, each of which was filled with different concentration of bony and contrast materials, as shown in Fig. 1a. The multi-contrast phantom contains three concentrations (*C1*, *C2*, *C3*) of three different contrast agents (*CA-1*, *CA-2*, and *CA-3*), coupled with three concentrations of  $K_2HPO_4$  (*b-1*, *b-2*, and *b-3*) to mimic the bone tissue. Second, an anthropomorphic abdomen phantom, 41 cm in width and 33 cm in height (in the axial direction), was also designed and used to validate the energy mapping approach (Fig. 1b).

It is worth taking into consideration that our model calculates the sinogram using 2D model of aforementioned phantoms. It means that the phantom shape, size, and contents are not changed by variation of slice thickness. Slice thickness variation only affects the photon intensity in our model.

The attenuation coefficient data of materials and tissues used in the phantoms were calculated using the WinXcom database software [49], reported in detail in our previous work [46].

We simulated nine different contrast agents: Bi (bismuth), Au (gold), Pt (platinum), W (tungsten), Ta (tantalum), Hf (hafnium), Yb (ytterbium), Er (erbium), and Gd (gadolinium), each at three different concentrations (see Table 1). The concentrations of the contrast agents were adjusted so as to match linear attenuation coefficient (LAC) values of all contrast agents for all energies between 1 and

**Table 1** Three levels of adjusted concentration of contrast agents (C1, C2 and C3) used in this work

Quantity	Materials (chemical symbols)									
	Gd	Er	Yb	Hf	Ta	W	Pt	Au	Bi	
Atomic number (Z)	64	68	70	72	73	74	78	79	83	
K-edge energy (keV)	50.2	57.5	61.3	65.4	67.4	69.5	78.4	80.7	90.5	
Density (g/cm <sup>3</sup> )	7.9	9.1	6.7	13.3	16.7	19.3	21.5	19.3	9.7	
C1 (mg/mL)	11.5	10.2	9.4	8.5	8.3	7.9	7.0	6.8	5.8	
C2 (mg/mL)	23.0	20.5	18.8	17.1	16.6	15.8	14.1	13.6	11.5	
C3 (mg/mL)	34.5	30.7	28.2	25.6	25.0	23.7	21.1	20.5	17.3	

**Table 2** Examinations performed and related acquisition protocols for the K-edge ratio imaging method

Examination	Contrast agents	Energy bin <sub>1</sub> (keV)	Energy bin <sub>2</sub> (keV)	Energy bin <sub>3</sub> (keV)	Energy bin <sub>4</sub> (keV)
1	Yb, Pt, Bi	50–60	63–77	80–89	92–102
2	Gd, Hf, Au	39–49	52–64	67–79	82–92
3	Er, W, Bi	46–56	59–68	71–89	92–102
4	Er, Ta, Au	46–56	59–66	69–79	82–92

The first and second numbers in each cell of energy bin columns represent the thresholds of energy bins

140 keV, except energies close to K-edge energies. This was for each of the three concentration groupings used. Our aim was to generate challenging situations for discrimination of the contrast agents from each other by conventional CT imaging.

#### Energy mapping based on integral-mode CT

For the single-kVp measurement, we used the tri-linear energy mapping method [50, 51] using the following equation:

$$\mu_{511} = \begin{cases} M_1 \cdot \text{HU} + N_1 & \text{HU} < 0 \\ M_2 \cdot \text{HU} + N_2 & 0 \leq \text{HU} < \text{HU}_{\text{bone}} \\ M_3 \cdot \text{HU} + N_3 & \text{HU} \geq \text{HU}_{\text{bone}} \end{cases} \quad (1)$$

where  $M$  and  $N$  denote the slope and intercept coefficients of the linear conversion equations which transform HU at CT energy to LAC at PET energy,  $\mu_{511}$ . The standard six coefficient values in the tri-linear mapping method above as used in commercial PET/CT scanners were employed for conversion of CT HU units to LAC in 511 keV [50, 51].

The tri-linear method was examined on the computerized anthropomorphic phantom containing three different contrast agents: Gd in two regions in the liver, Hf as blood pool in the aorta and in the colon, and Au in the stomach (Examination 2 in Table 2); we also placed a calcification on the aortic wall, all simultaneously.

For the dual-kVp CT measurements, we used the DE<sub>slope</sub> method [39, 52, 53]: a coordinate system with 80 kVp HU

on the vertical  $Y$ -axis against 140 kVp HU on the horizontal  $X$ -axis was formed.

The DE<sub>slope</sub> method was applied on the anthropomorphic phantom containing the same materials used in single-kVp mode (described above). The slopes of fitted lines on bony and contrast agent pixel values were measured. The slope of the separation line, used to distinguish between regions containing contrast agent from bony regions in the formed coordinate system, was calculated by averaging the slopes of bone and contrast agent lines. The values of the extracted contrast agent pixels were replaced with the value for water to produce virtual none contrast (VNC) image. To obtain the attenuation map at 511 keV, the VNC image was transformed to 511 keV using a bi-linear energy mapping function having the coefficients given in Eq. (1) except that the third equation was removed and the constraint on the second equation changed to  $\text{HU} \geq 0$ .

#### Energy mapping based on spectral CT

We used our previously proposed image-based K-edge ratio method [46] in which the image acquired from the energy window located above the K-edge energy is divided by the image acquired from the energy window located below the K-edge energy. By dividing these two images, a parametric map (virtual image) is generated, i.e.

$$R_{\text{K-edge}} = \frac{\text{Im}(\text{bin}_i)}{\text{Im}(\text{bin}_j)}, \quad (2)$$

where  $\text{Im}(\text{bin}_i)$  and  $\text{Im}(\text{bin}_j)$  are the images reconstructed using data gathered in energy windows  $\text{bin}_i$  and  $\text{bin}_j$ , respectively, which straddle the K-edge energy.

Due to the sudden increase in the LAC just above the K-edge energy, the effective LAC in the energy window above the K-edge is noticeably higher than that below the K-edge energy. Therefore, in spite of the general trend for LACs, in which the LAC at higher energies is smaller than that in lower energies, the value of ratio near K-edge is larger than unity. Since each contrast agent material has a unique K-edge energy (Table 1), by specifying appropriate energy windows around the K-edge energy, each contrast

material can be segmented and identified even when several contrast agents are present simultaneously.

In total, four examinations using multi-contrast and anthropomorphic phantoms were performed, each one with a different combination of contrast agents as described in Table 2. When using the multi-contrast phantom, three concentrations of each contrast agent (C1, C2, and C3) together with three concentrations of  $K_2HPO_4$  (100, 350, and 700 mg/cc) were used. When using the anthropomorphic phantom, we put two different concentrations of Gd in two regions within the liver, two different concentrations of Hf as blood pool in the aorta and in the colon, and Au in the stomach. In Table 2 we summarized acquisition protocols for all examinations. For designing the acquisition protocols, we assumed that the energy resolution of the detector might not be ideal. Therefore, we left a 3 keV gap between the high edge of one bin and the low edge of the following one as used in Ref. [33] to avoid contrast-to-noise ratio degradations due to overlapping of adjacent energy windows. After selecting an appropriate acquisition protocol, the images corresponding to each energy bin were reconstructed.

By applying Eq. (2) on the reconstructed images,  $R_{K-edge}$  parametric maps were generated. For instance, in examination 1 (Table 2), the ytterbium, platinum, and bismuth can be discriminated by calculation of  $R_{61.3}$ ,  $R_{78.4}$ , and  $R_{90.5}$  which are the parametric maps achieved by dividing  $bin_2$  by  $bin_1$ ,  $bin_3$  by  $bin_2$  and  $bin_4$  by  $bin_3$ , respectively. In these parametric maps the pixels corresponding to the contrast agents are expected to exhibit values higher than unity and all other pixels lower than unity.

To generate the VNC image, we used the following equation:

$$\text{VNC Image} = \begin{cases} \text{diagnostic Image,} & R_{K-edge} \leq 1 \\ \text{Water,} & R_{K-edge} > 1 \end{cases}, \quad (3)$$

where *diagnostic Image* is an image originally reconstructed using the entire X-ray spectrum. By using Eq. (3) the  $R_{K-edge}$  parametric map is used to segment the regions containing contrast agents and replace by LAC of water in the diagnostic image, which leads to generating corresponding VNC image. Once the VNC image is generated, it should be transformed to the desired energy (511 keV for PET and 140 keV for SPECT) to obtain attenuation map. To this end, Eq. (1) can be used to transform VNC image to the attenuation map, where only two types of materials, air–water and water–bone mixtures, as representative of body tissues without any contrast agents, are considered. It means that by removing contrast agent in the VNC image, tri-linear energy mapping function of Eq. (1) should be reduced to bi-linear energy mapping function by removing

third equation and changing the constraint on the second equation to  $HU \geq 0$ .

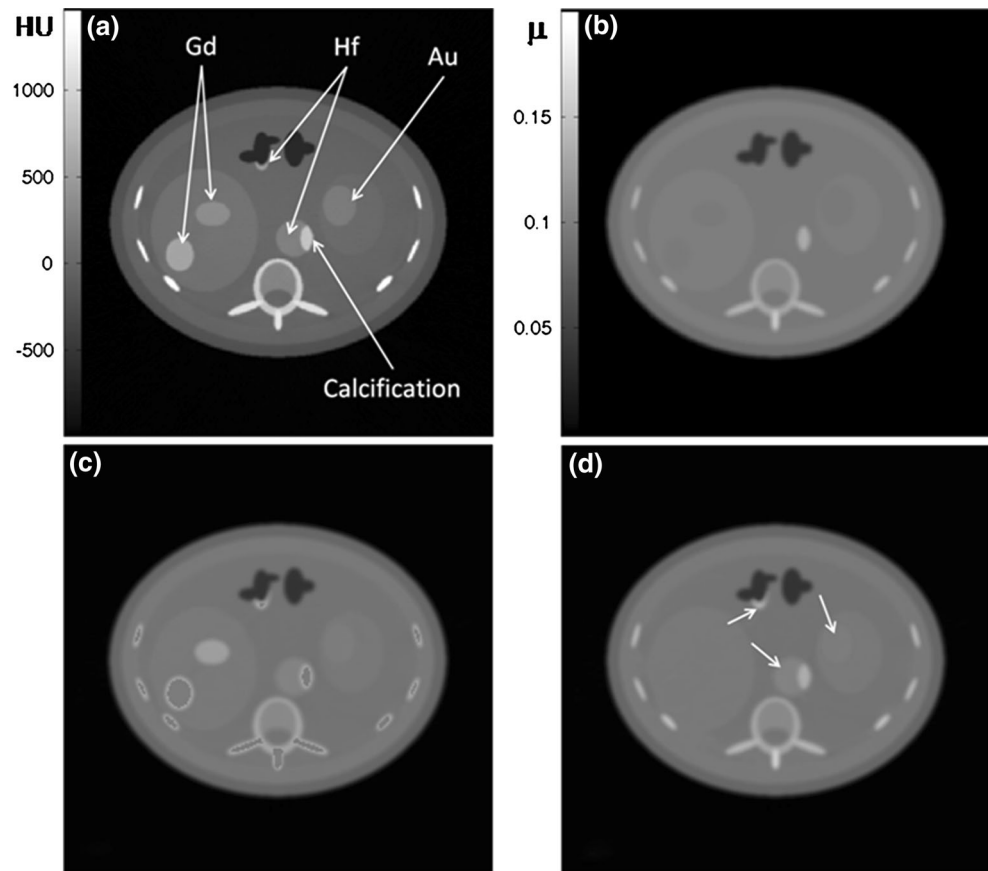
## Results

### Energy mapping based on integral mode CT

Simulated images of the anthropomorphic phantom (with contrast agents of examination 2) are shown in Fig. 2. The location of contrast agents and aortic calcifications are pointed by arrows in the integral mode CT image (Fig. 2a). The true attenuation map at 511 keV is shown in Fig. 2b, whereas Fig. 2c illustrates the attenuation map calculated using the single-kVp tri-linear algorithm. It can be seen that highly dense bony materials, such as spine blade, ribs and aortic calcifications are mistakenly transformed as contrast agents due to their very high HU values, while the cancellous bone and cortex of spine are correctly segmented. Moreover, one of the Gd regions in liver, the Hf blood pool in aorta, and the Au region in stomach are mistakenly segmented as bone due to their small HU values. In addition, it can be seen that simple thresholding normally used in tri-linear approach mischaracterizes most of the boundaries which have distinct pixel values due to the partial volume effect.

The dual-energy CT was also examined to generate the attenuation map at 511 keV of the multi-contrast phantom and anthropomorphic phantom (Fig. 2d). Unlike in the case of single-kVp tri-linear method, the  $DE_{slope}$  method could successfully discriminate different concentrations of bony materials. When mapping the multi-contrast phantom images by dual-energy CT method, we noticed that the slopes of a given contrast agent vary noticeably as function of the K-edge energy values when the  $DE_{slope}$  method is used. In the Table 3 the measured HU values of three concentrations of different contrast agents and related slopes are summarized. As can be seen in Table 3, when K-edge energy of contrast agents is below the effective energy of 80 kVp (typically 58 keV) the slope value is higher than bone (Gd and Er materials). However, other materials with higher K-edge energies have slope values smaller than that bone. Consequently, defining a unique separation line to discriminate all contrast agents listed in Table 2 is unfeasible. This means that when several contrast agents are scanned simultaneously, each with a different K-edge energy lying between or outside the dual-kVp effective energies, this approach is generally unlikely to be able to discriminate each one from bone tissues using the  $DE_{slope}$  method. Therefore, the resulting attenuation maps at 511 keV may contain contrast agent-related artifacts.

**Fig. 2** Anthropomorphic phantom study: **a** CT image and location of simultaneous contrast agents (*Gd*, *Hf*, and *Au*), **b** true attenuation map at 511 keV, **c** attenuation map at 511 keV calculated using the single-kVp tri-linear method, **d** attenuation map at 511 keV calculated using the  $DE_{\text{slope}}$  method



The attenuation map of the anthropomorphic phantom obtained using the  $DE_{\text{slope}}$  method, shown in Fig. 2d, demonstrates enhanced performance compared to the single-kVp tri-linear method (Fig. 2c). All bone regions with low or high densities as well as the calcification in the aorta are segmented and transformed correctly. Nevertheless, it can be seen that this method was not successful in discriminating all contrast agents. It was found that both Gd regions in the liver were well transformed at 511 keV energy with a relative difference  $<3\%$ , while this method failed for Hf and Au regions transformation resulting in relative differences exceeding  $18\%$ . The pitfalls are identified by arrows in Fig. 2d. The Gd regions were correctly discriminated from bone because its slope is larger than that of bone. Therefore, a separation line which lays between bone and Gd slopes is able to discriminate between them. However, the slopes of Hf and Au are less than the slope of bone due to their K-edge energies and thus cannot be discriminated by the above defined separation line.

#### Energy mapping based on spectral CT

Images of the multi-contrast phantom containing Yb, Pt, Bi agents with 61.3, 78.4, and 90.5 keV K-edge energies,

respectively, as reconstructed from detected photons in energy bins reported in Table 2 are shown in Fig. 3. As can be directly seen in Fig. 3a, the pixel values for the three contrast agents are almost identical in images obtained at the first energy bin (50–60 keV) when this energy is below all K-edge energies. As explained above, this is because we purposefully adjusted the concentrations of the agents so as to match their LACs. In the image obtained using the second energy bin (63–77 keV) shown in Fig. 3b, the pixel values of regions containing Yb increase (5, 8, and 11 O'clock) because in this bin the average energy is higher than the Yb K-edge energy. It can be seen in Fig. 3c that pixels obtained using the third energy bin (80–89 keV) located in regions containing Pt (4, 7, 10 O'clock) exhibit higher values than when the acquisition is performed using the two previous bins. Similarly, for the images obtained in the fourth bin (92–102) shown in Fig. 3d, where the bin energy is higher than the Bi K-edge energy, the regions containing this contrast agent (3, 6 and 9 O'clock) show increased values. The regions containing bony materials (12, 1 and 2 O'clock) have nearly similar values to contrast agent in some images but the trend of falling LAC values versus energy is preserved owing to the absence of K-edge in the energy range of the images.

**Table 3** Mean and standard deviation of CT numbers in HU (measured on  $15 \times 15$ -pixel size ROIs) of different contrast agents with C1, C2 and C3 concentrations (see Table 1) at (80 kVp, 150 mAs) and (140 kVp, 250 mAs) images of multi-contrast phantom, along with the slopes of the fitted line on the 80 vs. 140 kVp coordinate system using the  $DE_{slope}$  method

kVp	Concentration	Contrast agents												
		Gd	Er	Yb	Hf	Ta	W	Pt	Au	Bi	Bone			
80	C1	565.9 ± 18.6	437.3 ± 13.4	350.9 ± 10.8	265.7 ± 8.5	238.2 ± 9.2	201.7 ± 6.0	136.3 ± 4.6	169.8 ± 5.3	146.9 ± 5.5	545.7 ± 20.5			
	C2	1102.4 ± 36.3	883.7 ± 27.1	676.4 ± 20.8	550.3 ± 17.7	460.7 ± 17.8	391.3 ± 11.7	309.3 ± 10.6	294.6 ± 9.2	290.1 ± 11.0	1071.3 ± 40.4			
	C3	1615.2 ± 53.1	1281.2 ± 39.3	996.8 ± 30.6	796.5 ± 25.7	679.7 ± 26.2	578.9 ± 17.3	437.8 ± 15.0	459.4 ± 14.4	431.5 ± 16.3	1524.4 ± 57.5			
140	C1	307.6 ± 10.1	287.5 ± 8.8	262.2 ± 8.0	230.0 ± 7.4	225.5 ± 8.7	206.5 ± 6.1	171.4 ± 5.8	210.0 ± 6.5	149.7 ± 5.6	359.5 ± 13.5			
	C2	580.3 ± 19.1	570.9 ± 17.5	504.7 ± 15.5	471.0 ± 15.2	431.2 ± 16.6	395.7 ± 11.8	381.0 ± 13.0	351.8 ± 11.0	285.1 ± 10.8	690.6 ± 26.0			
	C3	824.7 ± 27.1	808.3 ± 24.8	732.7 ± 22.5	670.4 ± 21.6	633.0 ± 24.4	583.4 ± 17.5	539.0 ± 18.4	544.4 ± 17.0	423.4 ± 16.0	973.8 ± 36.7			
Slope of fitted line		2.03	1.62	1.37	1.20	1.08	1.00	0.82	0.87	1.04	1.59			

The calculated  $R_{K-edge}$  parametric maps of the multi-contrast phantom containing Yb, Pt, Bi contrast agents are shown in Fig. 4. It can be seen that the regions containing the contrast agent with the corresponding  $R_{K-edge}$  exhibit higher gray values compared to other regions so they can be segmented by applying simple thresholding. The results obtained using  $R_{61.3}$  show that only regions containing Yb have pixel values greater than unity (Fig. 4a). Similarly, those obtained using  $R_{78.4}$  and  $R_{90.5}$  show that only regions containing Pt and Bi, respectively, produce pixel values higher than unity (Fig. 4b, c).

Figure 5a shows the diagnostic CT image of the anthropomorphic phantom containing Gd, Hf, and Au contrast agents. In Fig. 5b the segmented contrast agents using K-edge ratio method are shown as colored overlay on the diagnostic image, where the Gd, Hf, and Au are represented by yellow, orange, and magenta colors. The VNC-based attenuation maps at 511 keV obtained using K-edge ratio method are shown in Fig. 5c. As can be seen in Table 4, the percentage relative difference using the ROI-based analysis between these attenuation maps and the true attenuation map is <2.5 %.

### Discussion

Although CT-based attenuation correction of PET data has several advantages, it still has a number of limitations that need to be resolved. The administration of contrast agent for diagnostic quality CT might result in noticeable bias in the generated attenuation maps in regions containing contrast media leading to SUV bias [1]. Several studies reported on the propagation of the bias from the attenuation maps into attenuation-corrected PET images [19–22, 24, 54, 55], and it has been shown that an increase in the concentration of iodine contrast agent leads to higher SUV values [53]. Clearly, this error will be more pronounced when higher atomic number NP contrast agents are used.

To improve the accuracy of the CTAC procedure, regions containing contrast agent on the CT image need to be accurately segmented to avoid overestimating PET attenuation maps following energy mapping. This fact coupled with considerable effort to introduce new CT contrast agents [3–17] to extend the capability of molecular imaging will provide a stimulus to research in the area of accurate differentiation of contrast agents in PET/CT imaging. It is important because newly introduced contrast agents have higher atomic numbers, thus pronouncing higher linear attenuation coefficients leading to higher artifact via CTAC.

The advantages of NP contrast agents in terms of long circulation times in the body and the ability to target specific cancer cells provide the possibility of targeted multi-

**Fig. 3** Multi-contrast phantom study: **a**  $\text{bin}_1 = 50\text{--}60$  keV; **b**  $\text{bin}_2 = 63\text{--}77$  keV; **c**  $\text{bin}_3 = 80\text{--}89$  keV, and **d**  $\text{bin}_4 = 92\text{--}102$  keV images of multi-contrast phantom filled with examination 1 materials (see Table 2). All pixels are in HU. All images have same *gray color bar* shown in (a)

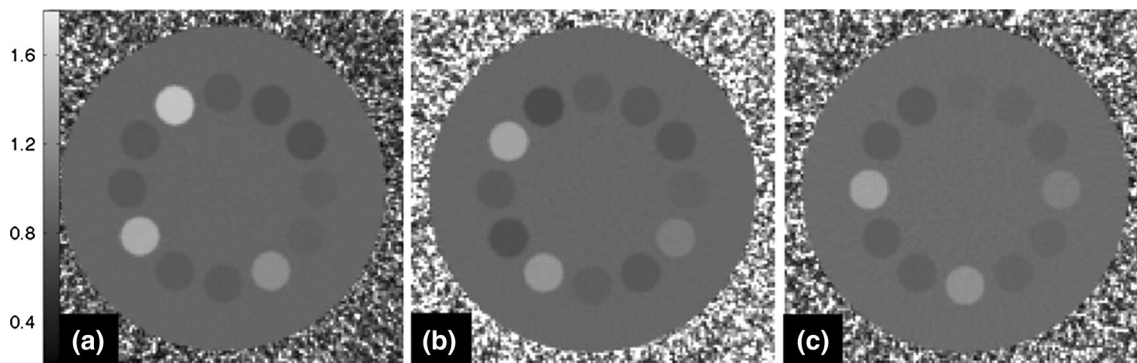
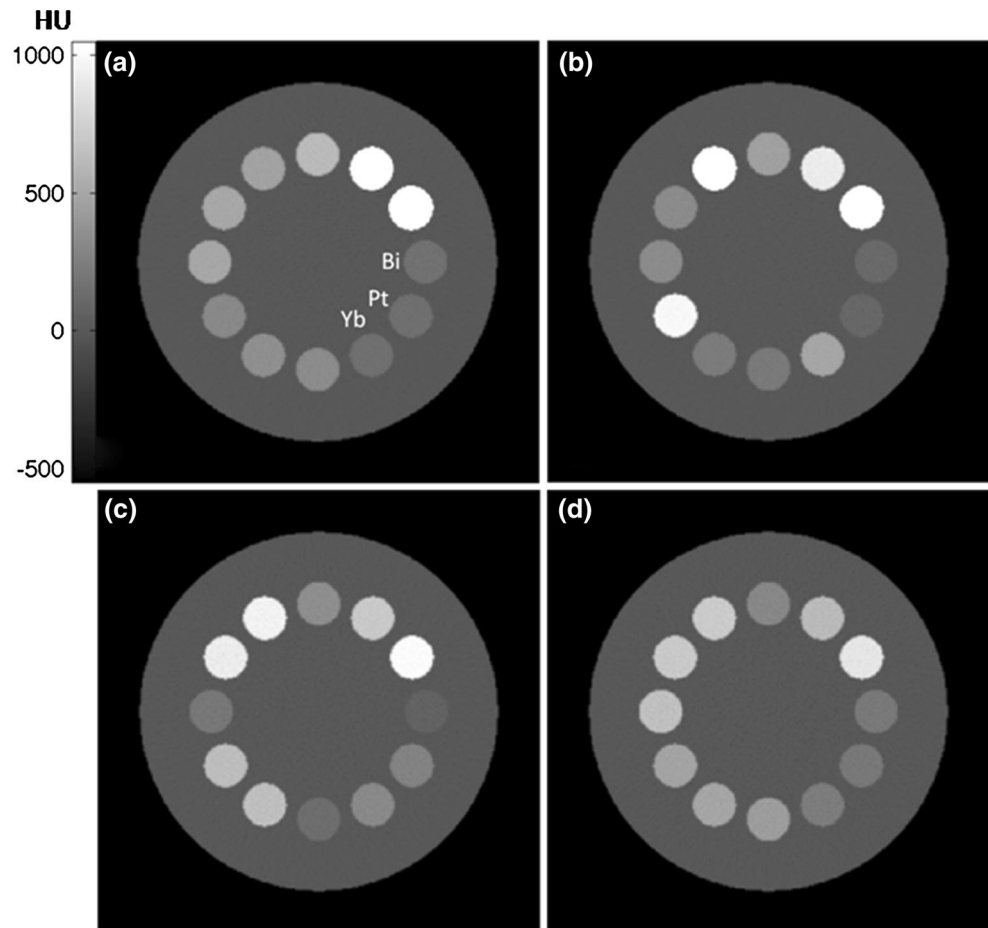


**Fig. 4** K-edge ratio parametric maps: **a**  $=\text{bin}_2/\text{bin}_1$ ; **b**  $=\text{bin}_3/\text{bin}_2$ , and **c**  $=\text{bin}_4/\text{bin}_3$  parametric maps of multi-contrast phantom images of Fig. 3. The contrast agents are differentiated in corresponding

parametric maps with pixel values greater than the unity. All images have same *gray color bar* shown in (a)

contrast molecular CT imaging, where multiple targetable contrast agents are administered. Thus, if enough time is allowed for accumulation in specific cells, a PET/molecular CT image can be obtained using a single CT scan [7, 18, 56].

In single-kVp CT, it is possible to have identical LACs for bone and contrast agent in CT images as a result of

large span of contrast agent concentrations and LACs in the body. This issue is increasingly more probable when using more than one contrast agent particularly in multi-contrast molecular CT imaging.

It has been shown that dual-kVp CT improves the ability to segment regions containing contrast agents. For example, when using methods such as dual-kVp slope, the extent

**Fig. 5** Anthropomorphic phantom study: **a** diagnostic CT image; **b** K-edge ratio colored overlay CT image of the anthropomorphic phantom filled with contrast agent materials in examination 2 (see Table 2) with segmented contrast agents: yellow gadolinium, orange hafnium and magenta gold; **c** VNC-based attenuation map at 511 keV derived using the K-edge ratio method (color figure online)

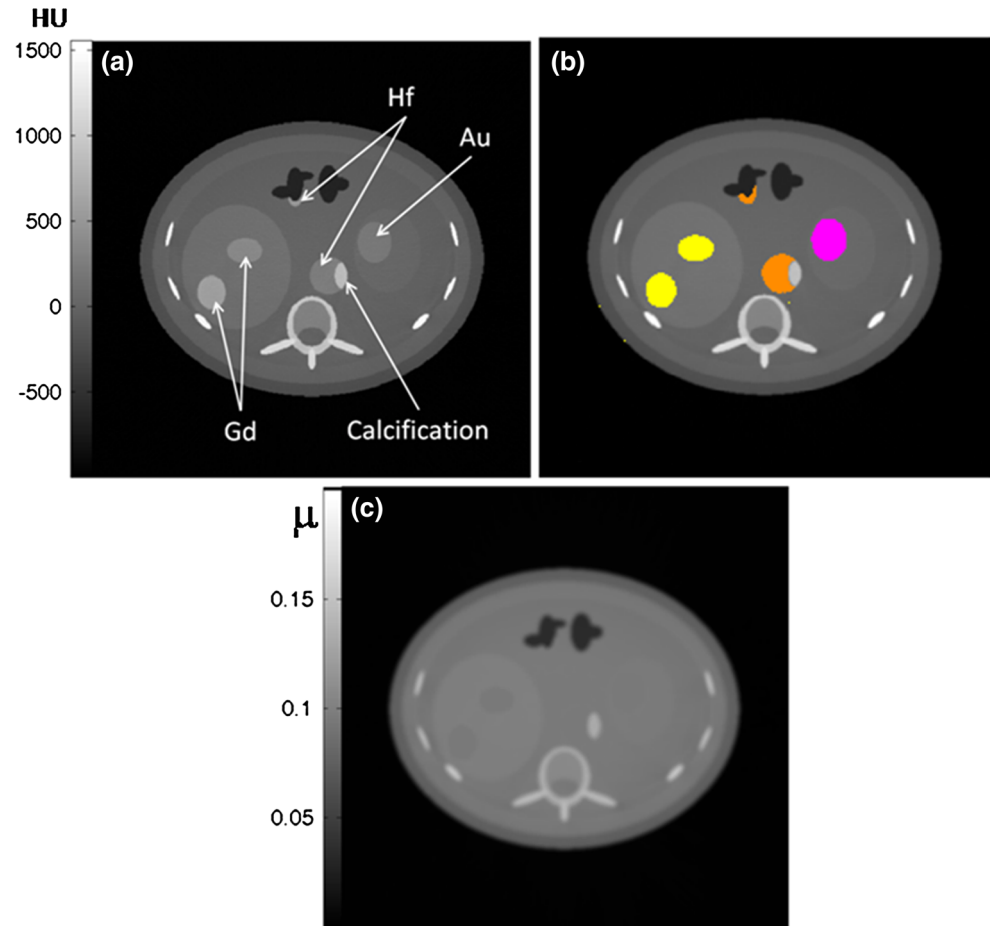


**Table 4** Percentage relative difference (RD %) of the VNC-based attenuation maps compared to true 511 keV attenuation map in the different ROIs of the anthropomorphic phantom

Region	VNC-based RD %
Bone	1.44
Calcification	2.47
Au-region	2.22
Hf-region	1.10
Gd-region	1.14

of errors introduced is reduced in applications involving a single contrast agent. In contrast, in the context of multi-contrast molecular CT imaging, we have shown that such an approach can fall very short of discriminating all contrast agents from bone as well as from each other (Table 3) because, in the case of using multiple contrast agents, it is unlike to define a unique separation line to discriminate all contrast agents simultaneously due to different K-edge energies of the contrast agent.

In this study, we examined previously proposed K-edge ratio imaging method [46] to differentiate multiple simultaneous contrast agents using multi-energy CT to suppress the inaccuracy in 511 keV attenuation map. Material

discrimination and/or identification has been investigated in a variety of aspects in several papers based on utilizing multi-energy (spectral) CT equipped with energy-sensitive photon-counting detectors [27, 32, 34–39]. Specifically, it has been demonstrated that it is possible to identify contrast agents with K-edge energies inside the radiologic energy scale by forming a system of simultaneous equations for multi-energy acquisition datasets, including decomposition of attenuation coefficients to energy-dependent functions, and iteratively solving such a system [32, 36–38]. Although such an approach has been reported to effectively discriminate contrast agents, solving a system of equations by iterative methods needs particular consideration to avoid ill-conditioning and divergence issues in the presence of multiple contrast agents with very similar LAC properties. In this approach, solving system of simultaneous equations should be repeated for each element of the sinogram (or each pixel of image in image domain approach) is very time consuming, especially in the cases in which large number of slices are acquired, i.e. three-dimensional (3D) whole body PET/CT analysis. Unlike most of previous K-edge imaging methods, which are based on projections, our proposed method is based on reconstructed images.

This method can discriminate and identify multiple contrast agents in the image domain using simple and direct calculations. In addition, our method does not need to determine constants and coefficients of particular functions such as photoelectric and Compton contributions, and as a result it does not require additional calibration procedures.

The results depicted in Fig. 5 demonstrate improved identification of contrast agents. Our proposed image-based K-edge ratio imaging is based on dramatic increases in the LACs at the K-edge energy of contrast agents. By forming a particular parametric map as the ratio of two images, one from the energy window above the K-edge energy and another from the energy window below the K-edge energy, the regions containing contrast agents will be individually recognized. By identifying contrast agent regions, the contrast agent artifacts can then be efficiently suppressed in CTAC of PET data.

The main limitation of our and others' K-edge imaging approaches, whether projection-based or image-based, is the dependence of the energy bin definitions on the K-edge energies of contrast agents. The energy binning should be designed such that no K-edge falls inside the bins and at the same time there should exist one bin below and one above the K-edge energy. This means that increasing the number of contrast agents leads to decreasing the energy bin widths. This requires enhanced detector energy resolutions; however, recent innovations in detector technology promise such sufficient energy resolution [33, 44, 57]. Furthermore, using narrower energy bins implies increasing quantum noise levels due to photon number starvation, although images reconstructed from the entire X-ray spectrum with high contrast-to-noise ratios can be used for diagnostic purposes instead. As such, as a compromise between the number of contrast agents to be simultaneously identified and the quantum noise of multi-bin images, an optimum point must be found for each application. At the same time, iterative image reconstruction algorithms have the promise to noticeably better address the photon limited nature of using increasingly narrow energy bins [58, 59], and as such, are expected to contribute to feasibility of multi-contrast agent CT imaging and CTAC applications.

The main limitations of our analytic modeling are that (a) it only works with simple geometric phantoms composed of primitive geometric objects. (b) The photon interactions and scattering are not directly modeled, and (c) the model does not support the cases with different region and object size when it is compensating beam hardening effect, which may lead to less accuracy in the complex geometries.

Although accurate beam-hardening correction considering all possible cases such as region size, object size, materials, and so on need more sophisticated algorithms, we

have considered beam hardening only based on a 25-cm water phantom calibration to avoid reduction of CT values in the center of phantoms. Beam-hardening correction on the reconstructed images of 25 cm water phantom obtained from our analytic CT simulator decreased the CT value's error from 8.5 to <1.0 % in the center of the water phantom. It worth mentioning that experimental validation of our model also showed acceptable accuracy in terms of different CT values and noise in the reconstructed images [46].

We also wish to emphasize that in cases in which a pixel may consist of more than one contrast agent, discrimination using Eq. (2) may be limited, especially when the K-edge energies of mixed materials are very close. To avoid such situations, the administered simultaneous contrast agents should be selected appropriately. When the K-edge energy differences of mixed materials are large enough compared to the energy bins width, the K-edge ratio method would be able to discriminate between the materials even when several of them are mixed. This is due to the fact that any material (i.e. contrast agent) has its unique K-edge energy, and being mixed does not affect the K-edge energy values. As such, this can be one advantage of the K-edge ratio method.

Finally, we found that standard contrast agents such as iodine and barium, due to their low K-edge energy, are not appropriate for the proposed K-edge imaging, especially for human applications, as they lead to very low photon counts in the energy windows below their K-edge energies. Our calculations showed that it is nearly impossible to obtain images with applicable signal-to-noise ratios from energy windows below the K-edge energy of iodine when the X-ray spectrum is filtered by the mm-scale of aluminum and attenuated by the human body.

In conclusion, we have examined the ability of an image-based K-edge ratio method using spectral CT to generate the 511-keV attenuation map in the presence of multiple nanoparticulate CT contrast agents for the purpose of CT-based attenuation correction of PET data, while allowing the generation of diagnostic quality CT images. The results show that the proposed image-based K-edge ratio method using spectral CT outperforms conventional single-kVp and dual-kVp approaches.

**Acknowledgments** This work was supported by Tehran University of Medical Sciences under Grant 21342 and the Swiss National Science Foundation under grant SNSF 31003A-149957.

## References

1. Boellaard R. Standards for PET image acquisition and quantitative data analysis. *J Nucl Med.* 2009;50(Suppl 1):11S–20S.
2. Abdoli M, Dierckx RA, Zaidi H. Metal artifact reduction strategies for improved attenuation correction in hybrid PET/CT imaging. *Med Phys.* 2012;39(6):3343–60.

3. Qu M, Ehman E, Fletcher JG, Huprich JE, Hara AK, Silva AC, et al. Toward biphasic computed tomography (CT) enteric contrast: material classification of luminal bismuth and mural iodine in a small-bowel phantom using dual-energy CT. *J Comput Assist Tomogr.* 2012;36(5):554–9.
4. Aviv H, Bartling S, Grinberg I, Margel S. Synthesis and characterization of Bi<sub>2</sub>O<sub>3</sub>/HSA core-shell nanoparticles for X-ray imaging applications. *J Biomed Mater Res B Appl Biomater.* 2013;101(1):131–8.
5. Cormode DP, Roessl E, Thran A, Skajaa T, Gordon RE, Schlomka JP, et al. Atherosclerotic plaque composition: analysis with multicolor CT and targeted gold nanoparticles. *Radiology.* 2010;256(3):774–82.
6. Reuveni T, Motiei M, Romman Z, Popovtzer A, Popovtzer R. Targeted gold nanoparticles enable molecular CT imaging of cancer: an in vivo study. *Int J Nanomed.* 2011;6:2859–64.
7. Clark DP, Ghaghada K, Moding EJ, Kirsch DG, Badea CT. In vivo characterization of tumor vasculature using iodine and gold nanoparticles and dual energy micro-CT. *Phys Med Biol.* 2013;58(6):1683–704.
8. Chou SW, Shau YH, Wu PC, Yang YS, Shieh DB, Chen CC. In vitro and in vivo studies of FePt nanoparticles for dual modal CT/MRI molecular imaging. *J Am Chem Soc.* 2010;132(38):13270–8.
9. Axelsson O. Inventor contrast agents comprising tungsten-containing cores. European patent EP1893243. March 2008.
10. Torres AS, Bonitatibus PJ Jr, Colborn RE, Goddard GD, Fitzgerald PF, Lee BD, et al. Biological performance of a size-fractionated core-shell tantalum oxide nanoparticle x-ray contrast agent. *Invest Radiol.* 2012;47(10):578–87.
11. Dekrafft KE, Boyle WS, Burk LM, Zhou OZ, Lin W. Zr- and Hf-based nanoscale metal-organic frameworks as contrast agents for computed tomography. *J Mater Chem.* 2012;22(35):18139–44.
12. Oh MH, Lee N, Kim H, Park SP, Piao Y, Lee J, et al. Large-scale synthesis of bioinert tantalum oxide nanoparticles for X-ray computed tomography imaging and bimodal image-guided sentinel lymph node mapping. *J Am Chem Soc.* 2011;133(14):5508–15.
13. Zhou J, Zhu X, Chen M, Sun Y, Li F. Water-stable NaLuF<sub>4</sub>-based upconversion nanophosphors with long-term validity for multimodal lymphatic imaging. *Biomaterials.* 2012;33(26):6201–10.
14. Pan D, Schirra CO, Senpan A, Schmieder AH, Stacy AJ, Roessl E, et al. An early investigation of ytterbium nanocolloids for selective and quantitative “multicolor” spectral CT imaging. *ACS Nano.* 2012;6(4):3364–70.
15. Liu Z, Li Z, Liu J, Gu S, Yuan Q, Ren J, et al. Long-circulating Er<sup>3+</sup>-doped Yb<sub>2</sub>O<sub>3</sub> up-conversion nanoparticle as an in vivo X-Ray CT imaging contrast agent. *Biomaterials.* 2012;33(28):6748–57.
16. Ashokan A, Menon D, Nair S, Koyakutty M. A molecular receptor targeted, hydroxyapatite nanocrystal based multi-modal contrast agent. *Biomaterials.* 2010;31(9):2606–16.
17. Liu Y, Ai K, Lu L. Nanoparticulate X-ray computed tomography contrast agents: from design validation to in vivo applications. *Acc Chem Res.* 2012;45(10):1817–27.
18. Bulte JW. Science to practice: can CT be performed for multi-color molecular imaging? *Radiology.* 2010;256(3):675–6.
19. Ay MR, Zaidi H. Assessment of errors caused by X-ray scatter and use of contrast medium when using CT-based attenuation correction in PET. *Eur J Nucl Med Mol Imaging.* 2006;33(11):1301–13.
20. Heusner TA, Kuehl H, Veit-Haibach P, Hahn S, Boy C, Forsting M, et al. Highly iodinated intravenous contrast material for PET/CT—a feasibility study. *Rofo.* 2008;180(8):740–5.
21. Kropil P, Budach W, Bolke E, Gerber PA, Zinnmann F, Hautzel H, et al. Pitfalls in radiation oncology. “Myocardial metastasis” in PET–CT after palliative radiation treatment of the left 5th rib. *Strahlenther Onkol.* 2012;188(4):359–62.
22. McKeown C, Dempsey MF, Gillen G, Paterson C. Quantitative analysis shows that contrast medium in positron emission tomography/computed tomography may cause significant artefacts. *Nucl Med Commun.* 2012;33(8):864–71.
23. Ahmadian A, Ay MR, Bidgoli JH, Sarkar S, Zaidi H. Correction of oral contrast artifacts in CT-based attenuation correction of PET images using an automated segmentation algorithm. *Eur J Nucl Med Mol Imaging.* 2008;35(10):1812–23.
24. Nehmeh SA, Erdi YE, Kalaigian H, Kolbert KS, Pan T, Yeung H, et al. Correction for oral contrast artifacts in CT attenuation-corrected PET images obtained by combined PET/CT. *J Nucl Med.* 2003;44(12):1940–4.
25. Zaidi H, Hasegawa B. Determination of the attenuation map in emission tomography. *J Nucl Med.* 2003;44(2):291–315.
26. Kinahan PE, Alessio AM, Fessler JA. Dual energy CT attenuation correction methods for quantitative assessment of response to cancer therapy with PET/CT imaging. *Technol Cancer Res Treat.* 2006;5(4):319–27.
27. Alvarez RE, Macovski A. Energy-selective reconstructions in X-ray computerized tomography. *Phys Med Biol.* 1976;21(5):733–44.
28. Lehmann LA, Alvarez RE, Macovski A, Brody WR, Pelc NJ, Riederer SJ, et al. Generalized image combinations in dual KVP digital radiography. *Med Phys.* 1981;8(5):659–67.
29. Flohr TG, McCollough CH, Bruder H, Petersilka M, Gruber K, Suss C, et al. First performance evaluation of a dual-source CT (DSCT) system. *Eur Radiol.* 2006;16(2):256–68.
30. Zou Y, Silver MD, editors. Analysis of fast kV-switching in dual energy CT using a pre-reconstruction decomposition technique. Proceedings of the SPIE medical imaging: physics of medical imaging, San Diego, CA; 2008.
31. Carmi R, Naveh G, Altman A, editors. Material separation with dual-layer CT. IEEE nuclear science symposium conference record. Wyndham El Conquistador Resort, Puerto Rico: IEEE; Oct 2005. pp 23–29.
32. Roessl E, Cormode D, Brendel B, Jürgen Engel K, Martens G, Thran A, et al. Preclinical spectral computed tomography of gold nano-particles. *Nucl Instrum Method A.* 2011;648:S259–64.
33. Koenig T, Schulze J, Zuber M, Rink K, Butzer J, Hamann E, et al. Imaging properties of small-pixel spectroscopic x-ray detectors based on cadmium telluride sensors. *Phys Med Biol.* 2012;57(21):6743–59.
34. Le HQ, Molloy S. Segmentation and quantification of materials with energy discriminating computed tomography: a phantom study. *Med Phys.* 2011;38(1):228–37.
35. Le Huy Q, Molloy S. Least squares parameter estimation methods for material decomposition with energy discriminating detectors. *Med Phys.* 2011;38(1):245–55.
36. Roessl E, Proksa R. K-edge imaging in x-ray computed tomography using multi-bin photon counting detectors. *Phys Med Biol.* 2007;52(15):4679–96.
37. Schlomka JP, Roessl E, Dorscheid R, Dill S, Martens G, Istel T, et al. Experimental feasibility of multi-energy photon-counting K-edge imaging in pre-clinical computed tomography. *Phys Med Biol.* 2008;53(15):4031–47.
38. Schmidt TG, Pektas F. Region-of-interest material decomposition from truncated energy-resolved CT. *Med Phys.* 2011;38(10):5657–66.
39. Wang X, Meier D, Taguchi K, Wagenaar DJ, Patt BE, Frey EC. Material separation in x-ray CT with energy resolved photon-counting detectors. *Med Phys.* 2011;38(3):1534–46.

40. Lee SW, Choi YN, Cho HM, Lee YJ, Ryu HJ, Kim HJ. A Monte Carlo simulation study of the effect of energy windows in computed tomography images based on an energy-resolved photon counting detector. *Phys Med Biol*. 2012;57(15):4931–49.
41. He P, Wei B, Cong W, Wang G. Optimization of K-edge imaging with spectral CT. *Med Phys*. 2012;39:6572.
42. Leng S, Yu L, Wang J, Fletcher JG, Mistretta CA, McCollough CH. Noise reduction in spectral CT: reducing dose and breaking the trade-off between image noise and energy bin selection. *Med Phys*. 2011;38(9):4946–57.
43. Herrmann C, Engel KJ, Wiegert J. Performance simulation of an x-ray detector for spectral CT with combined Si and Cd[Zn]Te detection layers. *Phys Med Biol*. 2010;55(24):7697–713.
44. Walsh MF, Opie AMT, Ronaldson JP, Doesburg RMN, Nik SJ, Mohr JL, et al. First CT using Medipix3 and the MARS-CT-3 spectral scanner. *J Instrum*. 2011;6:C01095.
45. Riederer SJ, Mistretta CA. Selective iodine imaging using K-edge energies in computerized x-ray tomography. *Med Phys*. 1977;4(6):474–81.
46. Ghadiri H, Ay MR, Shiran MB, Soltanian-Zadeh H, Zaidi H. K-edge ratio method for identification of multiple nanoparticulate contrast agents by spectral CT imaging. *Br J Radiol*. 2013;86(1029):20130308.
47. Cranley K, Gilmore B, Fogarty G, Desponds L, Sutton D. Catalogue of diagnostic x-ray spectra and other data. IPEM report 78. 1997.
48. Ghadiri H, Shiran MB, Soltanian-Zadeh H, Rahmim A, Ay MR. A fast and hardware-mimicking analytic CT simulator. *IEEE nuclear science symposium and medical imaging conference, Korea*; 2013.
49. Gerward L, Guilbert N, Jensen KB, Leving H. WinXCom—a program for calculating X-ray attenuation coefficients. *Radiat Phys Chem*. 2004;71(3–4):653–4.
50. Abella M, Alessio AM, Mankoff DA, MacDonald LR, Vaquero JJ, Desco M, et al. Accuracy of CT-based attenuation correction in PET/CT bone imaging. *Phys Med Biol*. 2012;57(9):2477–90.
51. Lonn AHR. Evaluation of method to minimize the effect of X-ray contrast in PET-CT attenuation correction. *IEEE nuclear science symposium, conference record*; 2004. pp. 2220–21.
52. Karlo C, Lauber A, Gotti RP, Baumuller S, Stolzmann P, Scheffel H, et al. Dual-energy CT with tin filter technology for the discrimination of renal lesion proxies containing blood, protein, and contrast-agent. An experimental phantom study. *Eur Radiol*. 2011;21(2):385–92.
53. Rehfeld NS, Heismann BJ, Kupferschlager J, Aschoff P, Christ G, Pfannenber AC, et al. Single and dual energy attenuation correction in PET/CT in the presence of iodine based contrast agents. *Med Phys*. 2008;35(5):1959–69.
54. Kadkhodayan S, Shahriari S, Treglia G, Yousefi Z, Sadeghi R. Accuracy of 18-F-FDG PET imaging in the follow up of endometrial cancer patients: systematic review and meta-analysis of the literature. *Gynecol Oncol*. 2013;128(2):397–404.
55. Lee SD, Kim SH, Kim YK, Kim C, Kim SK, Han SS, et al. (18)F-FDG-PET/CT predicts early tumor recurrence in living donor liver transplantation for hepatocellular carcinoma. *Transpl Int*. 2013;26(1):50–60.
56. Shilo M, Reuveni T, Motiei M, Popovtzer R. Nanoparticles as computed tomography contrast agents: current status and future perspectives. *Nanomedicine (Lond)*. 2012;7(2):257–69.
57. Procz S, Pichotka M, Lubke J, Hamann E, Ballabriga R, Blaj G, et al. Flatfield correction optimization for energy selective X-ray imaging with Medipix3. *IEEE Trans Nucl Sci*. 2011;58(6):3182–9.
58. Singh S, Kalra MK, Do S, Thibault JB, Pien H, Connor OO, et al. Comparison of hybrid and pure iterative reconstruction techniques with conventional filtered back projection: dose reduction potential in the abdomen. *J Comput Assist Tomogr*. 2012;36(3):347–53.
59. Deak Z, Grimm JM, Treitl M, Geyer LL, Linsenmaier U, Korner M, et al. Filtered back projection, adaptive statistical iterative reconstruction, and a model-based iterative reconstruction in abdominal CT: an experimental clinical study. *Radiology*. 2013;266(1):197–206.